



OPEN

Light-driven oxygen evolution from water oxidation with immobilised TiO₂ engineered for high performance

Maria J. Sampaio^{1✉}, Zhipeng Yu^{1,2}, Joana C. Lopes¹, Pedro B. Tavares³, Cláudia G. Silva¹, Lifeng Liu² & Joaquim L. Faria¹

Calcination treatments in the range of 500–900 °C of TiO₂ synthesised by the sol–gel resulted in materials with variable physicochemical (i.e., optical, specific surface area, crystallite size and crystalline phase) and morphological properties. The photocatalytic performance of the prepared materials was evaluated in the oxygen evolution reaction (OER) following UV-LED irradiation of aqueous solutions containing iron ions as sacrificial electron acceptors. The highest activity for water oxidation was obtained with the photocatalyst thermally treated at 700 °C (TiO₂-700). Photocatalysts with larger anatase to rutile ratio of the crystalline phases and higher surface density of oxygen vacancies (defects) displayed the best performance in OER. The oxygen defects at the photocatalyst surface have proven to be responsible for the enhanced photoactivity, acting as important active adsorption sites for water oxidation. Seeking technological application, water oxidation was accomplished by immobilising the photocatalyst with the highest OER rate measured under the established batch conditions (TiO₂-700). Experiments operating under continuous mode revealed a remarkable efficiency for oxygen production, exceeding 12% of the apparent quantum efficiency (AQE) at 384 nm (UV-LED system) compared to the batch operation mode.

Oxygen is used in numerous industrial processes, for example, synthesis of chemicals, petroleum processing, glass, ceramic, pulp and paper manufacture. It is mainly used to enhance the reaction rates and to ensure the complete oxidation of possible undesired by-products occurring during some processes¹. Unfortunately, the transport and delivery of gaseous molecular oxygen pose several trends to its industrial application. Production in situ is undoubtedly an alternative forwarded by many technological strategies.

Therefore, the demand for oxygen production has encouraged the scientific community to expand the concept of artificial photosynthesis that mimics nature to convert solar energy into value-added products. Since the pioneering work of Fujishima and Honda in 1972², reporting the development of a photoelectrochemical cell for the decomposition of water into hydrogen and oxygen under UV light irradiation using the optical semiconductor titanium dioxide (TiO₂), research in this field became an important topic both for environmental decontamination and energy conversion. A variety of optical semiconductors (e.g., TiO₂, zinc oxide (ZnO), tungsten trioxide (WO₃), graphitic carbon nitride (g-C₃N₄), bismuth-based materials, black phosphorus, and others) have been employed in several photoactivated applications, including degradation of domestic and industrial sewage, and conversion of natural resources, such as carbon dioxide, nitrogen, and water to value-added chemical and fuels^{3–10}.

Concerning water splitting using semiconductor photocatalysis, the process consists of two half-catalytic redox reactions, i.e., the hydrogen evolution reaction (HER) and the oxygen evolution reaction (OER), which are described by the following Eqs. (1) and (2), respectively:



¹Laboratory of Separation and Reaction Engineering – Laboratory of Catalysis and Materials (LSRE-LCM), Departamento de Engenharia Química, Faculdade de Engenharia, Universidade do Porto, Rua Dr. Roberto Frias s/n, 4200-465 Porto, Portugal. ²Clean Energy Cluster, International Iberian Nanotechnology Laboratory (INL), Avenida Mestre Jose Veiga, 4715-330 Braga, Portugal. ³Departamento de Química, Centro de Química-Vila Real, Universidade de Trás-os-Montes e Alto Douro, 5001-911 Vila Real, Portugal. ✉email: mjsampaio@fe.up.pt



The OER is viewed as a bottleneck for the energy conversion due to its slow kinetics¹¹, which involves four proton-coupled electron transfer steps. These elementary stages (i.e., charge carrier generation, separation and migration) occur during the photocatalytic water oxidation, followed by the surface catalytic reaction. Many efforts have been pursued on developing photocatalysts to accelerate the water oxidation, such as junction construction of metal oxides and by metal deposition, aiming to decrease the energy barrier^{10,12}. Despite the significant advances in photocatalysts development neat TiO₂ continues to receive particular attention due to the nature of the physical interactions between anatase and rutile crystalline phases, which may result in unique trap states and therefore can have a significant impact on the interparticle carrier transport¹³.

Although the catalyst nature is of high importance concerning the water splitting systems, the major limitation is its relatively low efficiency in the presence of pure water, requiring the addition of sacrificial agents. Thus, many examples exist of sacrificial molecules as electron donors to improve hydrogen production in solar-driven water splitting systems^{14–16}. However, only a limited variety of electron acceptors have been considered concerning OER. The frequently used electron acceptors are silver cations (Ag⁺), yet some problems arise from their use, i.e., generally, the photocatalytic formation of molecular oxygen is accompanied by the deposition of metallic silver (Ag⁰) nanoparticles, causing irreversible optical changes on the semiconductor properties. Slightly, ferric ions (Fe³⁺) have been employed as sacrificial electron acceptors to produce oxygen^{17,18} owing to its lower redox potential in water (+0.77 V; vs. NHE) over Ag⁺ (+0.80 V; vs. NHE), and due to the reversible redox couple Fe³⁺/Fe²⁺ in the aqueous phase compared with the Ag⁺ ions. The influence of Fe³⁺ ions as electron acceptors was documented by Matsumura group¹⁷. In this study, the authors used a TiO₂ rutile material for water oxidation and found that the reaction is favoured by superior adsorption of Fe³⁺ ions on TiO₂ over the Fe²⁺ ions.

Therefore, due to the crucial importance of O₂ in various processes this work explores in situ oxygen production by water oxidation based on semiconductor photocatalysis technology. The influence of oxygen defects, optical and crystalline properties of TiO₂ samples calcined at different temperatures was investigated for oxygen evolution using a low concentration of Fe³⁺ aqueous solution rather than the typical electron acceptor (Ag⁺). The lower price, high abundance and broad availability of iron compared to silver, the use of Fe³⁺/Fe²⁺ in low concentrations, makes this a cost-effective and sustainable process. In addition, considering the advantages of using continuous mode systems, a selected TiO₂ sample was deposited in a glass support, and the rate of oxygen production was assessed. To the best of our knowledge, this is the first study on photocatalytic water oxidation using immobilised TiO₂ towards in situ oxygen production under continuous mode, avoiding the need of recovery the catalyst as an additional step.

Results and discussion

X-ray diffraction (XRD) analysis was performed to determine the crystalline phase and crystallite size of TiO₂ samples (Fig. 1, Table 1). The peaks appearing at 25° and 48°, correspond to the lattice planes of 101 and 200 (JCPDS 21-1272) of TiO₂ anatase phase. The peaks at 27°, 36° and 54° with lattice planes of 110, 101 and 211 (JCPDS 21-1276), respectively reveal the presence of rutile phase. As displayed in Fig. 1 the diffraction peaks of both anatase and rutile phases of TiO₂ samples become intense as the calcination temperature increases, suggesting that TiO₂ samples are composed of irregular polycrystalline materials, and the crystallinity for both phases is improved by rising the temperatures.

Representative SEM images were obtained to visualise the morphology of the different TiO₂ samples (Fig. 2). Results reveal an irregular shape of TiO₂ particles with the increase of the calcination temperature. For TiO₂-500 and TiO₂-600 (Fig. 2a,b), spherical-like TiO₂ particles are observed with distinct sizes aggregate into clusters. At temperatures over 700 °C, it seems that small particles coalesce to form larger particles (Fig. 2c), due to the transformation of anatase into rutile phase (Fig. 1). At 900 °C the transformation of anatase–rutile is completed and agglomerations of more a uniform size of TiO₂ particles are noticed (Fig. 1e).

The TEM and high-resolution transmission electron microscopy (HRTEM) were used to further investigate the microstructure and composition of representative TiO₂ sample (TiO₂-700, Fig. 2c). In this case, the particles show a typical size of ca. 100 nm, for its crystallized phase (Fig. 1c-i, c-ii, respectively). In Fig. 2c-iii, the disordered layers on the surface of the TiO₂-700 sample are visible and marked with orange dashed lines, suggesting the presence of defects that can provide higher carrier concentration and more active sites¹⁹.

HRTEM image revealed well-resolved crystal lattices in a representative TiO₂-700 (Fig. 3c-iv), and the interplanar spacing values of 0.32, 0.35 nm correspond to the (110) and (101) crystal planes of rutile and anatase TiO₂, respectively, verifying the co-existence of rutile and anatase in a single nanoparticle, consistent with the XRD results.

Specific surface areas of TiO₂ samples were determined by nitrogen adsorption at 77 K (Table 1). As expected, the results show a decrease of S_{BET} with the enhancement of the calcination temperature, agreeing with the SEM observations.

The TiO₂ samples were examined by PL spectroscopy at room temperature under an excitation energy of 4.43 eV (280 nm) to investigate the incidence of charge separation upon light excitation (Fig. 3). The intense PL emission in the UV and visible regions is commonly attributed to excitons recombination and the presence of defect sites, respectively²⁰. The samples TiO₂-500 (Fig. 3a) and TiO₂-600 (Fig. 3b) show a broad peak at 3.0 eV ascribed to the crystallinity of TiO₂. By increasing the annealing temperature (samples c, d and e), a noticeable red shift is observed for 2.93 eV, suggesting that the TiO₂-700, TiO₂-800 and TiO₂-900 samples exhibited higher crystallinity, as confirmed by HRTEM observations (Fig. 2). Additionally, these strong peaks (2.93 and 3.00 eV) have been ascribed to the self-trapped excitons in anatase and free excitons in rutile, respectively²⁰. The peaks at

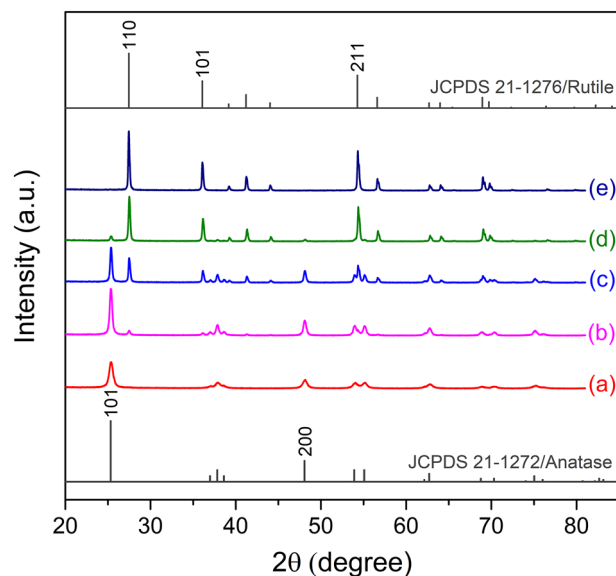


Figure 1. XRD diffractograms of TiO₂ samples: TiO₂-500 (a), TiO₂-600 (b), TiO₂-700 (c), TiO₂-800 (d) and TiO₂-900 (e).

Sample	Anatase (A)/rutile (R) ratio (%)	Crystallite size (nm) (A)	Crystallite size (nm) (R)	S _{BET} (m ² g ⁻¹)	Bandgap (eV)	Oxygen defects (%)
TiO ₂ -500	–	19.4	–	36.8	3.28	16.8
TiO ₂ -600	57.8	17.4	30.1	24.6	3.27	24.5
TiO ₂ -700	88.8	43.7	49.2	17.1	3.13	31.7
TiO ₂ -800	73.1	25.3	34.6	8.3	3.08	30.7
TiO ₂ -900	–	–	43.7	6.2	3.05	26.1

Table 1. Crystallisation parameters, specific surface area (S_{BET}), bandgap and oxygen defects of TiO₂ samples.

2.63–2.82 eV arise from the excitation electrons/holes recombination via oxygen vacancies and defects in both anatase and rutile phases of TiO₂.

The diffuse reflectance spectra of the TiO₂ samples were performed (Fig. 3b) and the respective bandgap values were obtained by indirect Tauc plot analysis (Table 1). As displayed, increasing the calcination temperature the bandgap of TiO₂ samples slightly diminish, which may indicate faster electron/hole recombination rates²¹.

We further have examined the surface chemical states of TiO₂ using XPS spectroscopy. Given that XPS allows investigating the surface atomic constituents, it has been used to characterise the degree of oxygen defect according to the relative element contents, and the intensities and positions of peaks^{22,23}. Among the defects identified in TiO₂, the presence of oxygen vacancies (O_v) can act as active adsorption sites, and strongly influence the reactivity of the photocatalysts²². Additionally, the formation of O_v commonly leads to the creation of unpaired electrons that can generate donor levels in the electronic structure of the TiO₂^{24,25}. As observed in Fig. 4 the O 1s XPS spectra of the TiO₂ samples were deconvoluted into three main peaks at 528.8 eV, 529.3 eV and 529.9 eV energies. The peak located at 528.8 eV is assigned to Ti–O–Ti bonding and lattice oxygen (O_L) within the TiO₂ structure²⁴. In contrast, the peaks at 529.3 eV and 529.9 eV energies are associated to surface chemisorbed hydroxyl groups (O_{ads}) and O_v, respectively. As displayed in Table 1, the area proportional to oxygen defects increase with the calcination temperature of TiO₂ samples until 700 °C (TiO₂-500, TiO₂-600, and TiO₂-700; 16.8%, 24.5%, and 31.7% respectively). For highest calcination temperatures (TiO₂-800, TiO₂-900; 30.7% and 26.1%, respectively) the oxygen defects start to decrease, suggesting that surface O_v concentration gradually diminishes with temperatures above 700 °C, being consistent with the literature^{24,26}.

Oxygen evolution reactions. Photocatalytic oxygen evolution was evaluated by TiO₂ samples calcined at various temperatures under UV-LED radiation using an aqueous Fe(NO₃)₃·9H₂O solution acting as sacrificial electron acceptor. Although the mechanism of O₂ evolution using silver cations (Ag⁺) as electron acceptors is well known in the literature^{15,27} the photocatalytic generation of molecular oxygen is followed by the deposition of metallic silver nanoparticles on the surface of the photocatalyst. Irreversible reactions accompany this phenomenon due to the plasmonic adsorption band of the silver particles¹⁵. Due to this issue and the high documented studies using Ag⁺ ions as sacrificial agent in photocatalytic water oxidation preliminary experiments were performed under the same operational conditions using this electron acceptor for comparison purposes

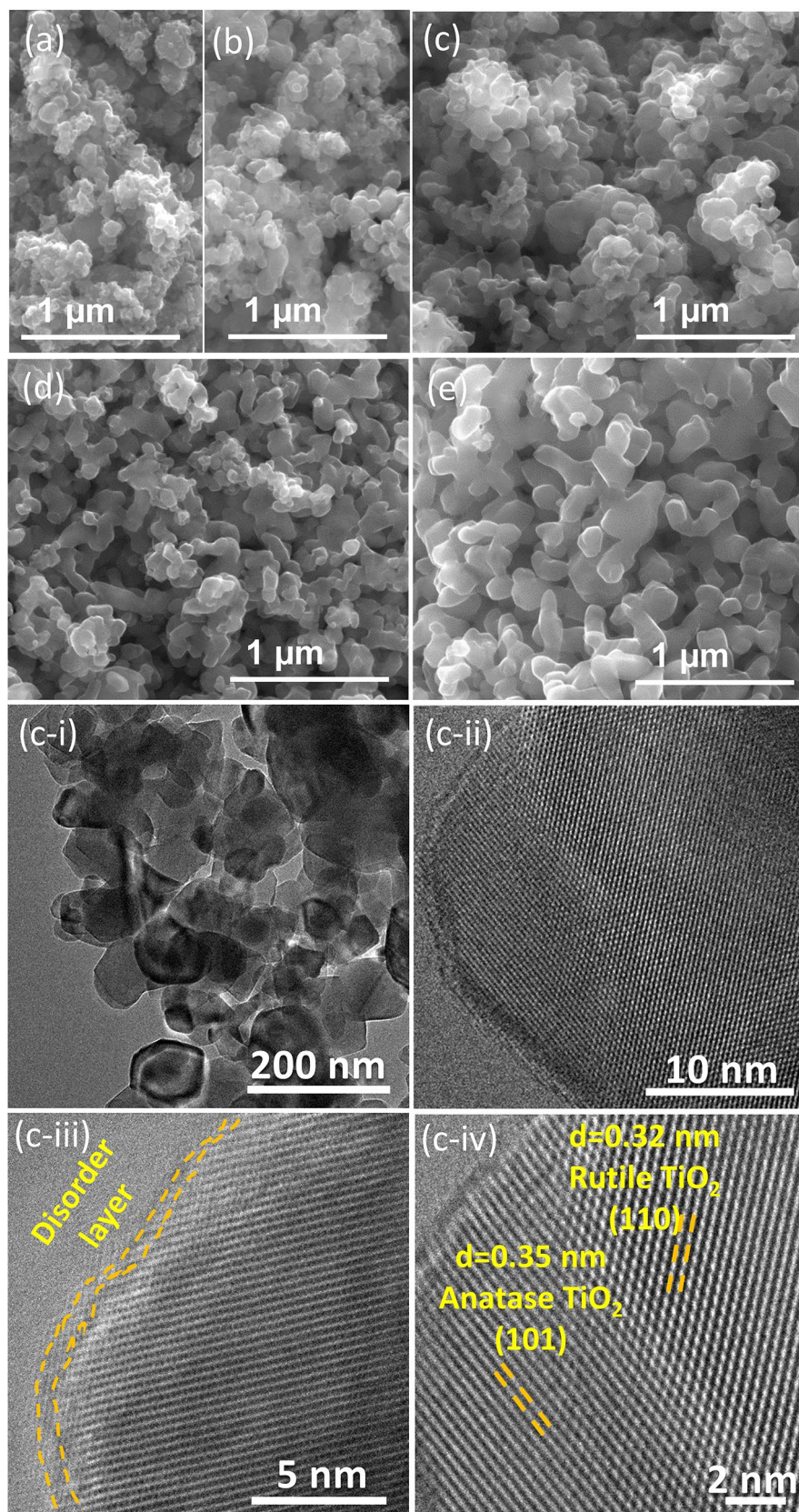


Figure 2. SEM images of TiO_2 samples: TiO_2 -500 (a), TiO_2 -600 (b), TiO_2 -700 (c), TiO_2 -800 (d) and TiO_2 -900 (e). Representative TEM and HRTEM images (c-i,ii,iii,iv) of TiO_2 -700 taken at different magnifications.

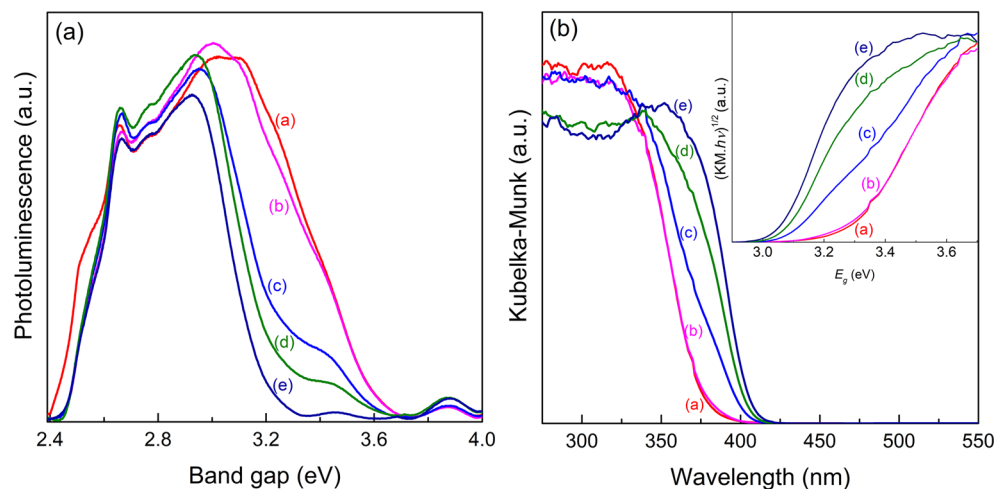


Figure 3. Photoluminescence (PL) spectra of TiO₂ samples (a), and DRUV-Vis and Tauc Plot (inset) for indirect bandgap (b): TiO₂-500 (a), TiO₂-600 (b), TiO₂-700 (c), TiO₂-800 (d) and TiO₂-900 (e).

(Supplementary Fig. S1). The results revealed a slight increasing efficiency for O₂ production in the first 30 min using Ag⁺ ions solution compared with the Fe³⁺. However, with the reaction time a progressive reduction of Ag⁺ into Ag⁰ and the oxygen evolution rates decreases.

Concerning the blank experiments (i.e., dark conditions, absence of catalyst and sacrificial agent), using a Fe³⁺ aqueous solution no formation of O₂ was noticed. Contrary, photocatalytic water oxidation reactions revealed that all the tested samples were found to generate O₂ upon UV-LED irradiation, although the efficiencies were dependent on the calcination temperature of TiO₂ samples (Fig. 5). In general, the results show that when the calcination temperature is raised, the efficiency of the photocatalytic process is enhanced. Nevertheless, after a specific temperature (800 °C), a decrease in O₂ evolution was observed. Among the photocatalysts, the TiO₂-700 sample showed the best performance for water oxidation with 8.95 μmol min⁻¹ g_{cat}⁻¹ of dissolved oxygen being detected.

The calcination treatment commonly affects the physicochemical properties of optical semiconductors, such as crystalline phase and crystallite size, specific surface area, and oxygen surface defects. Therefore, it is commonly accepted that a higher specific surface area (S_{BET}) promotes a significant number of active adsorption sites and improves reactivity. Yet, from the results it is unlikely that the efficiency of the TiO₂ samples is related to their specific surface area once was found a decrease in the S_{BET} with the rise of the calcination temperature. This diminution on the S_{BET} was more noticeable for the samples calcined at 800 and 900 °C due to the enhancement of the TiO₂ particles size as observed by SEM micrographs (Fig. 2). Additionally, the presence of higher percentage of rutile phase in these samples may indicate faster electron/hole recombination, which may explain the decrease in the efficiency of the water oxidation process²⁴.

Although in terms of oxygen evolution, effect of the particle size and the crystallite phases of the photocatalysts is not clearly understood, some reports suggest that these factors may contribute to the efficiency of photocatalytic water oxidation. Hiroshi et al.²⁸, ascribed the performance of the water oxidation photocatalytic process to the crystallization from anatase to rutile phase. More recently, Maeda et al.²⁹ have attributed the high efficiency of TiO₂ catalysts for oxygen evolution to the enhancement of the particle size which seems to hinder the electron/hole recombination. Higher efficiencies for O₂ production have been assigned to the TiO₂ rutile phase unlike what happens in the degradation of organic compounds using TiO₂ anatase^{30,31}. To understand the efficiency of the developed TiO₂ samples in terms of crystallization, experiments using commercial 100% TiO₂ anatase and 100% rutile were tested under the same experimental conditions (Fig. 5; A and R, respectively). As shown, high efficiency was found with the commercial TiO₂ rutile. Nevertheless, for the synthesised TiO₂ calcined at 900 °C 100% rutile (Table 1) the performance for O₂ production was lower compared with the TiO₂-700 and also with TiO₂-800 samples, suggesting that the other factors account to the efficiency of the process using the TiO₂ samples prepared by sol-gel method. As documented, the ratio between surface anatase and rutile particles increases the photocatalytic activity in water splitting reactions^{32,33}. As displayed in Fig. 6, the performance of the photocatalytic water oxidation for O₂ evolution was achieved when the ratio between anatase and rutile crystalline phases are superior (88%, Table 1), corroborating with the reported investigations^{33,34}.

It is recognised that lattice defects such as oxygen vacancies (O_v) can provide intermediate band levels or additional states into the forbidden band of the semiconductor that may trap electrons, which can increase the light absorption capacity and charge separation^{29,35}. Moreover, the high density of O_v (electron donors) is thought to shift the Fermi level of photocatalysts such as TiO₂ near the conduction band, enabling the charge separation at the TiO₂ particle interface, thus enhancing the degree of band bending at the semiconductor surface. Although the thermal treatments are known to increase the density of O_v, above a certain temperature, the number of O_v is reduced^{19,24,29}. Amano et al.³³ investigated the photocatalytic activity of a TiO₂ commercial sample treated at 700 °C under H₂ flow. The authors ascribed the photocatalytic performance to an increase in the density of the oxygen vacancies at the photocatalyst surface, which enhanced the electrons availability in the conduction band.

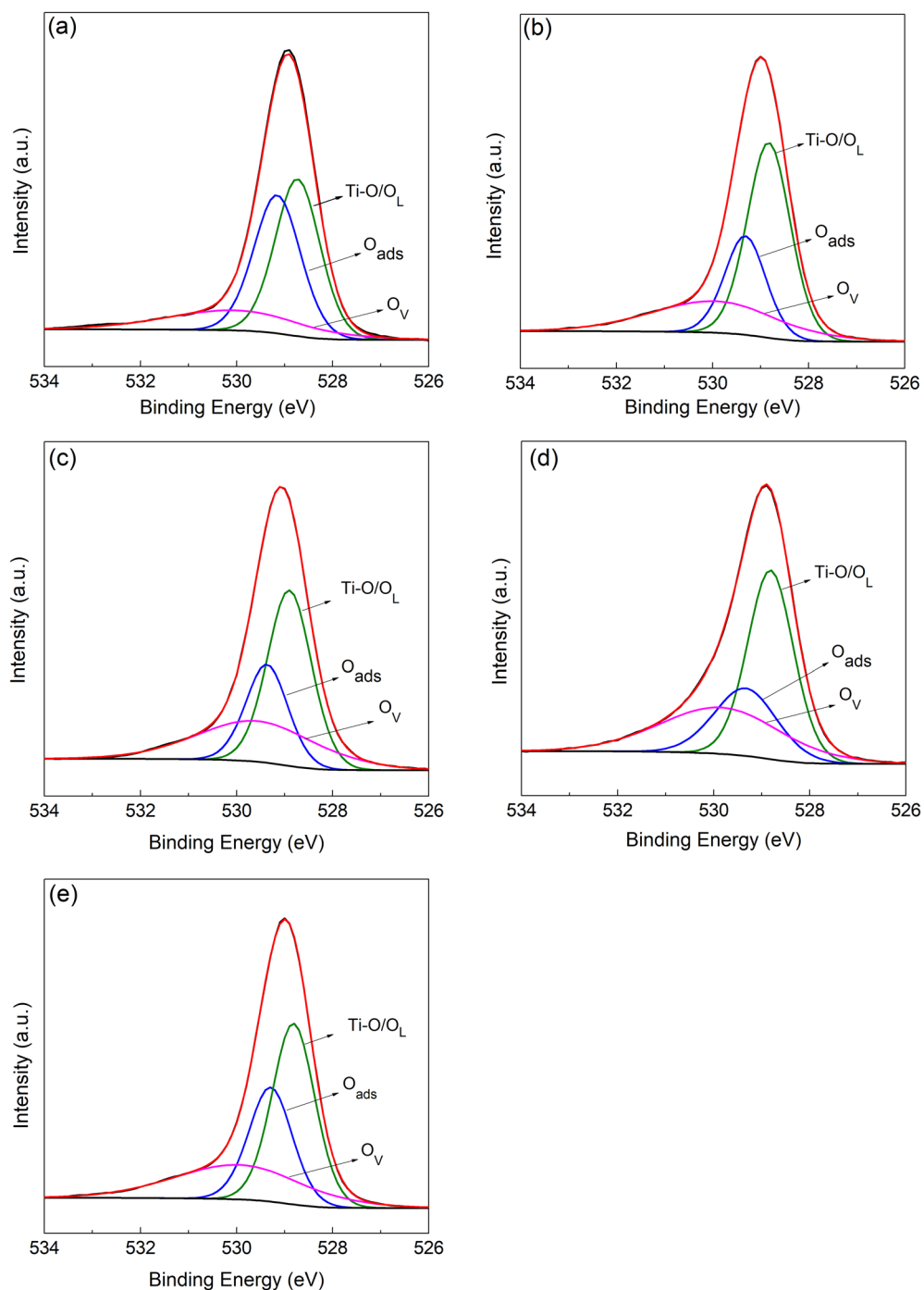


Figure 4. XPS spectra of the TiO₂ samples: TiO₂-500 (a), TiO₂-600 (b), TiO₂-700 (c), TiO₂-800 (d) and TiO₂-900 (e). O_v, O_L and O_{ads} correspond to oxygen vacancies, lattice oxygen and surface chemisorbed hydroxyl groups, respectively.

Regarding the characterisation results, it can be inferred that the high reactivity of the TiO₂-700 sample for water oxidation is due to the higher percentage of oxygen vacancies at the catalyst surface as was found by XPS analysis. This higher density of oxygen vacancies may facilitate the charge carrier diffusion in TiO₂, improving the photocatalytic activity for O₂ production. Although, the percentage of oxygen vacancies in the TiO₂-800 sample (30.7%) is negligible compared with the TiO₂-700 sample (31.7%), a decrease in the rutile particle size was observed (Table 1). The same behaviour was detected for TiO₂-900, i.e., smaller rutile particle size than the TiO₂-700, suggesting that excess thermal treatment is being used to decrease the oxygen vacancies, leading to the

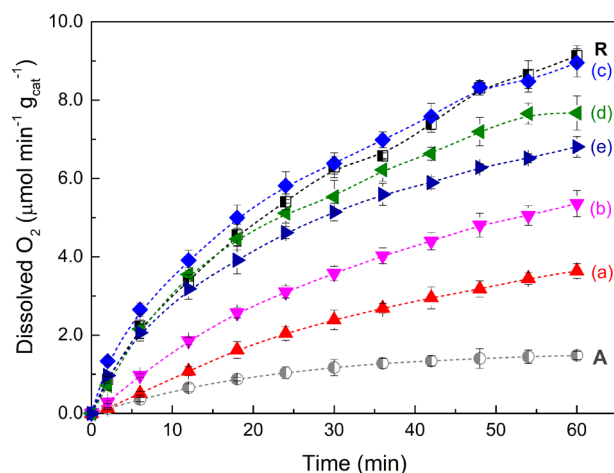


Figure 5. Photocatalytic dissolved oxygen evolution using TiO₂-500 (a), TiO₂-600 (b), TiO₂-700 (c), TiO₂-800 (d) and TiO₂-900 (e); n = 3 (standard deviation < 5%). R and A correspond to commercial TiO₂ 100% rutile and 100% anatase, respectively.

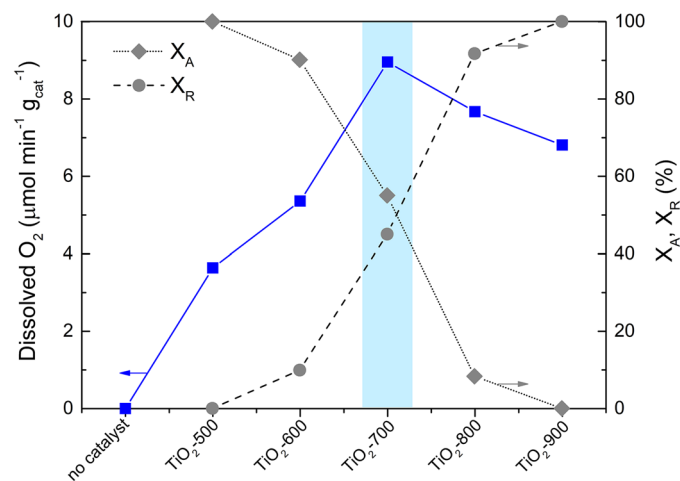
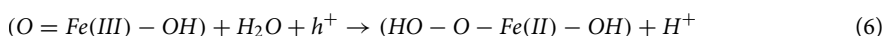
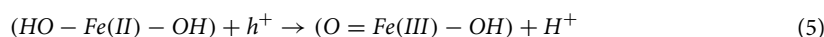
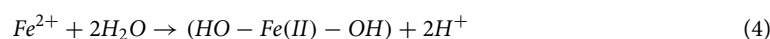
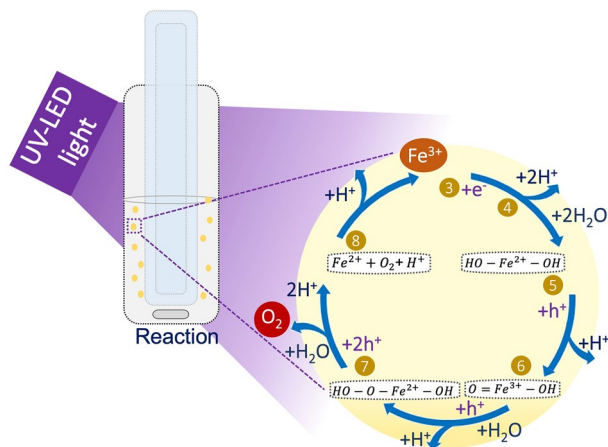


Figure 6. Photocatalytic dissolved oxygen evolution using TiO₂ samples calcined at different temperatures (left side), and percentage of anatase and rutile phases (right side).

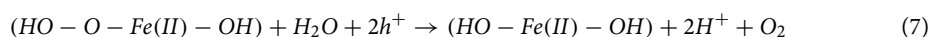
photocatalytic decreasing performance, being reliable with literature²⁶. Additionally, tries to obtain electrochemical evidence of the oxidation potential of the photocatalysts were performed by supporting the TiO₂ samples on conductive ITO electrode. The TiO₂-700 and TiO₂-800 samples (Supplementary Fig. S2) revealed an oxidation peak between 0.5 and 0.7 V vs SCE, suggesting that positive holes can be generated in the photocatalysis process, compatible with the observed results for photocatalytic oxygen production³⁶.

As described above, a significant number of investigations have been devoted to understanding the photocatalytic water oxidation using Ag⁺ cations as sacrificial electron acceptors, yet, using Fe³⁺ aqueous solutions few reports have been documented. Concerning the results obtained with the TiO₂ samples using the Fe³⁺ ion solutions it seems reasonable to propose that the overall process is governed by the mechanism illustrated in Scheme 1, and by the following equations:

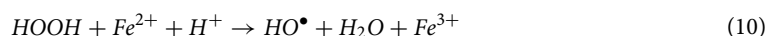
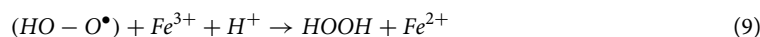
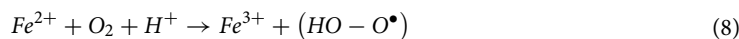




Scheme 1. Schematic representation of a proposed mechanism for O_2 evolution from $Fe(NO_3)_3 \cdot 9H_2O$ water solution under UV-LED light irradiation using TiO_2 photocatalysts. The numbers from 3 to 8 pair with Eqs. (3)–(8).



Additionally, as the O_2 is being accumulated in the reaction system the oxidation of Fe^{2+} into Fe^{3+} may also occur (Eq. (8)). Although in practice the oxidation in acid media is hard, at a moderate pH the iron(III) oxide hydrate (Fe_2O_3) can precipitate, and a reduction reaction of Fe^{3+} to Fe^{2+} can take place quickly (Eq. (9)). As a result, hydrogen peroxide (HO_2H) could be formed, occurring again the oxidation of Fe^{2+} into Fe^{3+} (Eq. (10)). Nevertheless, this last hypothesis seems to be challenging to occurs, as the maximum pH measured during the reactions was ca. 2.28.



Although the set of Eqs. (3)–(7) seems to describe the results obtained with the TiO_2 samples, a maximum amount of oxygen was evaluated after 60 min in the reaction conditions; after that, the reaction system achieved the steady state (Supplementary Fig. S3). This can be ascribed to the reaction system configuration used, i.e., as the process performance was evaluated in terms of in situ O_2 generation with the product remaining in reaction, which may indicate the O_2 solubility in the aqueous media was reached.

Therefore, considering the above results, a potential technological application for oxygen production was assessed using the TiO_2 -700 immobilised in a glass slide and tested under continuous mode (Supplementary Scheme S1b). Using this reactor configuration we can overcome the practical problems that arise from using a catalyst in powder form and ensure continuous feed of sacrificial electron acceptors. The apparent quantum efficiency (AQE) was examined for both reaction systems by the following equation:

$$AQE = \frac{4 \times n \times N_A \times h \times c}{A \times I \times t \times \lambda}$$

where n is the amount of O_2 molecules, N_A the Avogadro constant, h the Plank constant, c the speed of light in vacuum (m/s), A the irradiated area (78.5 and 19.8 cm^2 , batch, and continuous systems, respectively), I the exposed irradiation intensity in each system, t the time of the reactions (s), and λ the wavelength of the monochromatic LED (384 nm).

As displayed in Fig. 7 a, after 60 min of reaction the concentration of O_2 is lower operating in continuous mode ($5.46 \mu mol \min^{-1} g_{cat}^{-1}$) comparing with slurry mode ($8.95 \mu mol \min^{-1} g_{cat}^{-1}$). Nevertheless, it is important to refer that a larger amount of catalyst per volume is used in the slurry system (0.120 g) in contrast with the continuous mode (0.013 g). Nevertheless, the results reveal that the immobilisation of TiO_2 -700 as film enables a remarkable efficiency for O_2 production, exhibiting AQE exceeding 12% (Fig. 7b) at 384 nm compared with the slurry mode. This configuration system may constitute a step forward for developing efficient and viable systems capable of producing O_2 in continuous-flow reactors, reducing the operating costs and allowing large-scale production.

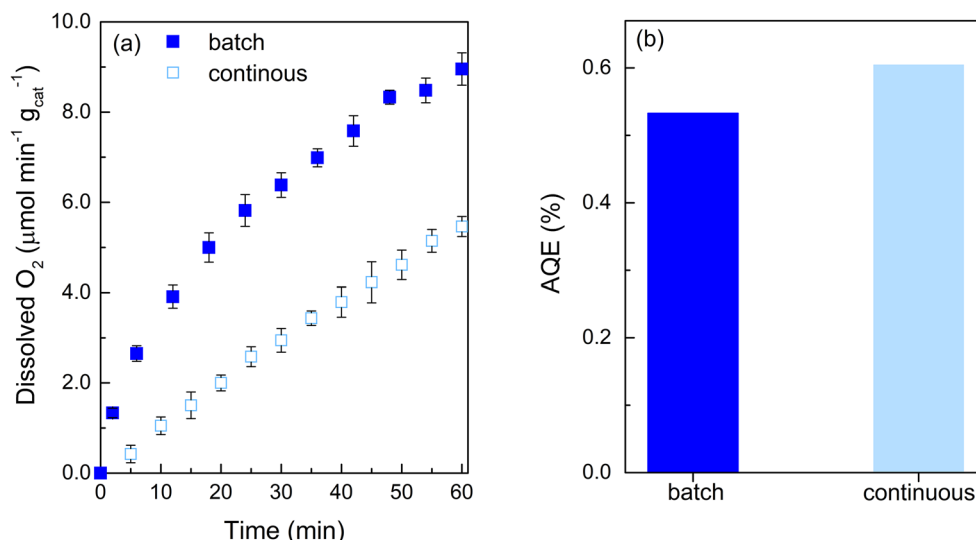


Figure 7. Comparison of oxygen evolution using batch and continuous mode reaction systems (a); $n = 3$ (standard deviation < 5%), and Apparent Quantum Efficiency (AQE) of the both reaction processes (b).

Conclusions

TiO₂ photocatalysts were synthesised by the sol–gel method and successfully used for water oxidation. High photocatalytic performance for oxygen evolution was achieved using iron nitride aqueous solution as sacrificial electron acceptors. Among the photocatalyst studied, the TiO₂-700 material revealed the highest efficiency with an in situ oxygen production rate of 8.95 μmol min⁻¹ g_{cat}⁻¹ being determined. The results were correlated with the physicochemical and morphological properties of the developed TiO₂ photocatalysts. The specific surface area of the resulting photocatalysts was found negligible for O₂ production, as well as the bandgap of the materials. The remarkable efficiency of the TiO₂-700 for oxygen evolution was correlated with the highest ratio between anatase and rutile phases (88%), which seems to indicate an efficient separation of the photogenerated electron/hole carriers. In addition, the superior reactivity of the TiO₂-700 sample was ascribed to the enhancing of the oxygen vacancies at the photocatalyst surface, which act as active sites for water oxidation.

Finally, the TiO₂-700 was successfully immobilised over a glass support for a continuous production of oxygen. The continuous-flow reaction system demonstrated promising results for water oxidation revealing a superior AQE at 384 nm compared with the results obtained in the batch system, 0.60 and 0.53, respectively.

Materials and methods

TiO₂ rutile (99%) was purchased from Iolitec. Iron(III) nitrate nonahydrate (≥ 98%; Fe(NO₃)₃·9H₂O), titanium butoxide (97%; Ti(OCH₂CH₂CH₂CH₃)₄), TiO₂ anatase (> 99%) and citric acid (≥ 99.5%; HOC(COOH)(CH₂COOH)₂) were supplied from Sigma-Aldrich. Absolute Ethanol (CH₃CH₂OH) was purchased from VWR. Ultrapure water was obtained from a Milli-Q water system (resistivity of 18.2 MΩ cm, at 25 °C).

Catalyst preparation and characterisation. Titanium dioxide samples were prepared from the sol–gel method: a solution with ethanol:titanium butoxide (50:3.5; molar ratio) was added drop-by-drop to a solution containing water:ethanol:citric acid (50:60:0.4; molar ratio) under continuous stirring. The final solution was kept mixed for 30 min followed by ageing in the air for several days, then the resulting xerogel was ground and dried at room temperature. The powders were calcined under the air atmosphere. Briefly, 1 g of powder was placed in a quartz crucible in a Microwave Phoenix apparatus (CEM Corporation) under static air conditions for 90 min at a given temperature. The final catalysts were designed as TiO₂-T, where T corresponds to the calcination temperature (between 500 and 900 °C).

Uncoated glass supports (7.6 × 2.6 cm) were extensively cleaned under sonication with an anionic detergent in water, followed by the immersion in 2-propanol for 15 min under sonication, and finally dried. A paste of a selected TiO₂-T sample was prepared as described in our previous work³⁷. The resulting photocatalyst paste was spread on the washed glass slides using the casting knife applicator (Elcometer 3580, Warren, MI). Then, the TiO₂-coated slides were calcined at 500 °C in static air for 3 h. The amount of catalyst immobilised was found from the difference between uncoated and coated slides after the calcination treatment.

X-ray diffraction (XRD) measurements were conducted in a PANalytical X'Pert MPD equipped with an X'Celerator detector and secondary monochromator (Cu Kα λ = 0.154 nm, 40 kV, 30 mA).

X-ray photoelectron spectroscopy (XPS) characterisation was carried out on an ESCALAB 250 instrument with Al Kα X-rays (1486.6 eV).

The morphology of the photocatalysts was examined by scanning electron microscopy (SEM) using a FEI Quanta 400 FEG ESEM/EDAX Genesis X4M (15 keV) microscope. High-resolution transmission electron

microscopy (HRTEM) was conducted on a probe-corrected transmission electron microscope operating at 200 kV (FEI Themis 60–300).

The N₂ adsorption–desorption isotherms at –196 °C were acquired in a Quantachrome NOVA 4200e device. The Brunauer–Emmett–Teller equation was used to obtain the specific surface area (S_{BET}) from the N₂ adsorption data in the relative pressure range 0.05–0.20 (Supplementary Fig. S4).

Diffuse Reflectance UV–Visible (DRUV-vis) spectra were obtained within the 220–800 nm wavelength range using a JASCO V-560 spectrophotometer equipped with an integrating sphere at room temperature. Photoluminescence (PL) analyses of the powder photocatalysts were attained at room temperature by a JASCO (FP 82000) fluorescence spectrometer with a 150 W Xenon lamp as a light source, using bandwidths of 10 nm for emission and excitation.

Photocatalytic water oxidation. Water oxidation experiments were conducted in a slurry glass-immersion reactor filled with 120 mL of 5 mM Fe(NO₃)₃·9H₂O solution acting as a sacrificial agent. Preliminary experiments were performed varying the initial concentration of the Fe(NO₃)₃·9H₂O solution between 1.0 and 50.0 mM (Supplementary Fig. S5). The photocatalytic system was maintained at ca. 20 °C using a cooling water system. In a typical experiment, TiO₂ powders were dispersed in the Fe(NO₃)₃·9H₂O solution and the resulting suspension (1 g L⁻¹) was completely deaerated by saturation with argon (50 mL min⁻¹) for 30 min. Then, the reactor headspace was maintained under the argon atmosphere (10 mL min⁻¹) to hinder oxygen gas–liquid transfer through the interface. The oxygen concentration was measured by an O₂-sensor FOXY probe (Ocean Optics NeoFOX) dipped in the suspensions. The photocatalytic reactor was exposed to a four LEDs system with a maximum wavelength of 384 nm (Supplementary Scheme S1a). The intensity of each LED varied between 120 and 127 W m⁻², which was measured at 3 cm from the reactor wall by a UV–Vis spectroradiometer apparatus (USB2000+, OceanOptics, USA).

Additional tests under continuous mode were performed using an acrylic reactor system with a maximum volume of 40 mL constituted by a chamber containing the immobilised TiO₂-700 film (0.013 g). The reactor was sealed and purged with an argon flow (10 mL min⁻¹) for ca. 2 h. The irradiation device, constituted by one LED source (λ_{max} = 384 nm; 127 W m⁻²), was used at 3 cm from the immobilised catalyst (Supplementary Scheme S1b). The reactor system was continuously fed with 5 mM of Fe(NO₃)₃·9H₂O solution previously saturated with argon. The residence time was kept at 20 min, taking into account the results obtained in batch mode. The accumulated dissolved oxygen was measured using an O₂-sensor FOXY probe.

Blank experiments were performed in all experiments, namely in the absence of catalysts, without adding sacrificial agents under illumination and dark conditions. All the reactions were carried out in triplicate.

Received: 10 August 2021; Accepted: 23 September 2021

Published online: 29 October 2021

References

- Thiemens, M. H. Oxygen origins. *Nat. Chem.* **4**, 66–66 (2012).
- Fujishima, A. & Honda, K. Electrochemical photolysis of water at a semiconductor electrode. *Nature* **238**, 37–38 (1972).
- Tang, J., Durrant, J. R. & Klug, D. R. Mechanism of photocatalytic water splitting in TiO₂. Reaction of water with photoholes, importance of charge carrier dynamics, and evidence for four-hole chemistry. *J. Am. Chem. Soc.* **130**, 13885–13891 (2008).
- Chen, X., Li, N., Kong, Z., Ong, W.-J. & Zhao, X. Photocatalytic fixation of nitrogen to ammonia: State-of-the-art advancements and future prospects. *Mater. Horiz.* **5**, 9–27 (2018).
- Kegel, J., Povey, I. M. & Pemble, M. E. Zinc oxide for solar water splitting: A brief review of the material's challenges and associated opportunities. *Nano Energy* **54**, 409–428 (2018).
- Liu, H. *et al.* Recent advances on black phosphorus for energy storage, catalysis, and sensor applications. *Adv. Mater.* **30**, 1800295 (2018).
- Ma, H. *et al.* Where do photogenerated holes at the g-C₃N₄/water interface go for water splitting: H₂O or OH⁻? *Nanoscale* **10**, 15624–15631 (2018).
- Moreira, N. F. F. *et al.* Metal-free g-C₃N₄ photocatalysis of organic micropollutants in urban wastewater under visible light. *Appl. Catal. B* **248**, 184–192 (2019).
- Gao, Y. *et al.* Recent advances in visible-light-driven conversion of CO₂ by photocatalysts into fuels or value-added chemicals. *Carbon Res. Conv.* **3**, 46–59 (2020).
- Lin, S., Huang, H., Ma, T. & Zhang, Y. Photocatalytic oxygen evolution from water splitting. *Adv. Sci.* **8**, 2002458 (2021).
- Curcio, A. *et al.* Unlocking the potential of mechanochemical coupling: Boosting the oxygen evolution reaction by mating proton acceptors with electron donors. *Adv. Funct. Mater.* **31**, 2008077 (2021).
- Li, D. *et al.* Unraveling the kinetics of photocatalytic water oxidation on WO₃. *J. Phys. Chem. Lett.* **11**, 412–418 (2020).
- Mi, Y. & Weng, Y. Band alignment and controllable electron migration between rutile and anatase TiO₂. *Sci. Rep.* **5**, 11482 (2015).
- Silva, C. G. *et al.* Photocatalytic production of hydrogen from methanol and saccharides using carbon nanotube-TiO₂ catalysts. *Appl. Catal. B* **178**, 82–90 (2015).
- Schneider, J. & Bahnemann, D. W. Undesired role of sacrificial reagents in photocatalysis. *J. Phys. Chem. Lett.* **4**, 3479–3483 (2013).
- Silva, C. G., Juárez, R., Marino, T., Molinari, R. & García, H. Influence of excitation wavelength (UV or visible light) on the photocatalytic activity of titania containing gold nanoparticles for the generation of hydrogen or oxygen from water. *J. Am. Chem. Soc.* **133**, 595–602 (2011).
- Ohno, T., Haga, D., Fujihara, K., Kaizaki, K. & Matsumura, M. Unique effects of iron(III) ions on photocatalytic and photoelectrochemical properties of titanium dioxide. *J. Phys. Chem. B* **101**, 6415–6419 (1997).
- Ohmori, T., Takahashi, H., Mametsuka, H. & Suzuki, E. Photocatalytic oxygen evolution on α-Fe₂O₃ films using Fe³⁺ ion as a sacrificial oxidizing agent. *Phys. Chem. Chem. Phys.* **2**, 3519–3522 (2000).
- Pham, H. H. & Wang, L.-W. Oxygen vacancy and hole conduction in amorphous TiO₂. *Phys. Chem. Chem. Phys.* **17**, 541–550 (2015).
- Mathew, S. *et al.* UV-visible photoluminescence of TiO₂ nanoparticles prepared by hydrothermal method. *J. Fluoresc.* **22**, 1563–1569 (2012).

21. Kim, M. G. *et al.* Effects of calcination temperature on the phase composition, photocatalytic degradation, and virucidal activities of TiO₂ nanoparticles. *ACS Omega* **6**, 10668–10678 (2021).
22. Hao, L., Huang, H., Zhang, Y. & Ma, T. Oxygen vacant semiconductor photocatalysts. *Adv. Funct. Mater.* **31**, 2100919 (2021).
23. Huang, X. *et al.* Impact of oxygen vacancies on TiO₂ charge carrier transfer for photoelectrochemical water splitting. *Dalton Trans.* **49**, 2184–2189 (2020).
24. Pan, X., Yang, M.-Q., Fu, X., Zhang, N. & Xu, Y.-J. Defective TiO₂ with oxygen vacancies: Synthesis, properties and photocatalytic applications. *Nanoscale* **5**, 3601–3614 (2013).
25. Zhang, Y. *et al.* Direct observation of oxygen vacancy self-healing on TiO₂ photocatalysts for solar water splitting. *Angew. Chem. Int. Ed.* **58**, 14229–14233 (2019).
26. Nishimoto, Y., Hasegawa, Y., Adachi, K. & Yamazaki, S. Factors affecting oxygen evolution through water oxidation on polycrystalline titanium dioxide. *RSC Adv.* **6**, 46994–47000 (2016).
27. Jeon, T. H. *et al.* Ag(I) ions working as a hole-transfer mediator in photoelectrocatalytic water oxidation on WO₃ film. *Nat. Commun.* **11**, 967 (2020).
28. Kominami, H., Murakami, S.-Y., Kato, J.-I., Kera, Y. & Ohtani, B. Correlation between some physical properties of titanium dioxide particles and their photocatalytic activity for some probe reactions in aqueous systems. *J. Phys. Chem. B* **106**, 10501–10507 (2002).
29. Maeda, K. Effects of the physicochemical properties of rutile titania powder on photocatalytic water oxidation. *ACS Catal.* **4**, 1632–1636 (2014).
30. Sun, Q. & Xu, Y. Evaluating intrinsic photocatalytic activities of anatase and rutile TiO₂ for organic degradation in water. *J. Phys. Chem. C* **114**, 18911–18918 (2010).
31. Luttrell, T. *et al.* Why is anatase a better photocatalyst than rutile?—Model studies on epitaxial TiO₂ films. *Sci. Rep.* **4**, 4043 (2014).
32. Zhang, J., Xu, Q., Feng, Z., Li, M. & Li, C. Importance of the relationship between surface phases and photocatalytic activity of TiO₂. *Angew. Chem. Int. Ed.* **47**, 1766–1769 (2008).
33. Amano, F., Nakata, M. & Ishinaga, E. Photocatalytic activity of rutile titania for hydrogen evolution. *Chem. Lett.* **43**, 509–511 (2014).
34. Li, Y.-F. & Selloni, A. Pathway of photocatalytic oxygen evolution on aqueous TiO₂ anatase and insights into the different activities of anatase and rutile. *ACS Catal.* **6**, 4769–4774 (2016).
35. Li, Y. *et al.* Photocatalytic water splitting by N-TiO₂ on MgO (111) with exceptional quantum efficiencies at elevated temperatures. *Nat. Commun.* **10**, 4421 (2019).
36. Han, F., Xu, J., Zhou, J., Tang, J. & Tang, W. Oxygen vacancy-engineered Fe₂O₃ nanoarrays as free-standing electrodes for flexible asymmetric supercapacitors. *Nanoscale* **11**, 12477–12483 (2019).
37. Sampaio, M. J., Silva, C. G., Marques, R. R. N., Silva, A. M. T. & Faria, J. L. Carbon nanotube–TiO₂ thin films for photocatalytic applications. *Catal. Today* **161**, 91–96 (2011).

Acknowledgements

This work was financially supported by Project POCI-01-0145-FEDER-030674 (MicroPhotOGen, PTDC/NAN-MAT/30674/2017) funded by ERDF through COMPETE2020—Programa Operacional Competitividade e Internacionalização (POCI)—and by national funds through FCT—Fundação para a Ciência e a Tecnologia. We would like to thank the scientific collaboration financially supported by: Base-UIDB/50020/2020 and Programmatic-UIDP/50020/2020 Funding of Associate Laboratory LSRE-LCM—funded by national funds through FCT/MCTES (PIDDAC), and when appropriate co-financed by FEDER under PT2020 Partnership Agreement: CQVR: UIDB/QUI/00616/2020. We are also indebted to MSc Rui Rocha and the CEMUP team (Portugal) for technical assistance and advice with SEM measurements.

Author contributions

M.J.S.: Conceptualization, Investigation, Funding acquisition, Methodology, Project administration, Supervision, Writing—review & editing original manuscript. Z.Y.: Formal analysis, Resources, Review & Editing. J.C.L.: Investigation, Formal analysis, Resources. P.B.T.: Formal analysis, Resources. C.G.S.: Methodology, Review & editing. L.L.: Formal analysis, Resources, Review & editing. J.L.F.: Conceptualization, Review & editing.

Competing interests

The authors declare no competing interests.

Additional information

Supplementary Information The online version contains supplementary material available at <https://doi.org/10.1038/s41598-021-99841-5>.

Correspondence and requests for materials should be addressed to M.J.S.

Reprints and permissions information is available at www.nature.com/reprints.

Publisher's note Springer Nature remains neutral with regard to jurisdictional claims in published maps and institutional affiliations.



Open Access This article is licensed under a Creative Commons Attribution 4.0 International License, which permits use, sharing, adaptation, distribution and reproduction in any medium or format, as long as you give appropriate credit to the original author(s) and the source, provide a link to the Creative Commons licence, and indicate if changes were made. The images or other third party material in this article are included in the article's Creative Commons licence, unless indicated otherwise in a credit line to the material. If material is not included in the article's Creative Commons licence and your intended use is not permitted by statutory regulation or exceeds the permitted use, you will need to obtain permission directly from the copyright holder. To view a copy of this licence, visit <http://creativecommons.org/licenses/by/4.0/>.

© The Author(s) 2021